

# Simultaneous Photocatalytic Oxygen Production and Hexavalent Chromium Reduction in $\text{Ag}_3\text{PO}_4/\text{C}_3\text{N}_4$ S-scheme Heterojunction

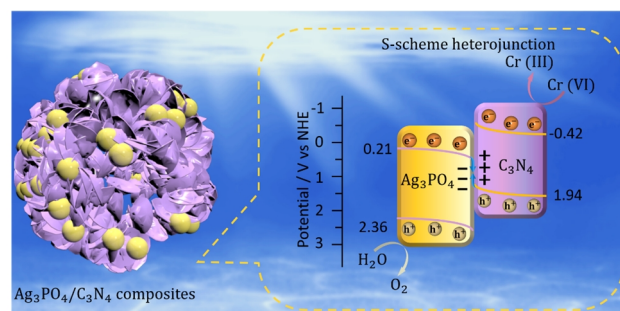
Tao Yang<sup>1†</sup>, Pengke Deng<sup>1†</sup>, Lele Wang<sup>1</sup>, Jie Hu<sup>1\*</sup>, Qinqin Liu<sup>1\*</sup> and Hua Tang<sup>1,2\*</sup>

<sup>1</sup>School of Materials Science & Engineering, Jiangsu University, Zhenjiang 212013, China

<sup>2</sup>School of Environmental Science and Engineering, Qingdao University, Qingdao 266071, China

**ABSTRACT** The low separation/migration efficiency is a major obstacle that limits the practical application of semiconductor-photocatalysts. Constructing S-scheme heterojunction is an ideal strategy for providing high photocatalytic activity via accelerating charge separation. Herein, an  $\text{Ag}_3\text{PO}_4/\text{C}_3\text{N}_4$  composite was synthesized by coupling  $\text{Ag}_3\text{PO}_4$  particle with  $\text{C}_3\text{N}_4$  hollow spheres in-situ via a precipitation method. The S-scheme heterojunction between  $\text{Ag}_3\text{PO}_4$  and  $\text{C}_3\text{N}_4$  could accelerate the charge separation and retain high photoredox ability, which synchronously realized high photocatalytic oxygen production and hexavalent chromium reduction. The optimized  $\text{Ag}_3\text{PO}_4/\text{C}_3\text{N}_4$  composite shows a high oxygen production rate up to  $803.31 \mu\text{mol}\cdot\text{g}^{-1}\cdot\text{h}^{-1}$  and a high conversion (87.9%) of  $\text{Cr(VI)}$  to  $\text{Cr(III)}$ . In addition,  $\text{C}_3\text{N}_4$  hollow spheres affords higher reaction efficiency than that of  $\text{C}_3\text{N}_4$  tube,  $\text{C}_3\text{N}_4$  bulk and  $\text{C}_3\text{N}_4$  sheet, which indicates that the hollow sphere structure can provide more active sites and adsorption sites in the photocatalytic process. This work offers an effective way in developing a dual-function S-scheme heterojunction for clean energy production and environmental protection.

**Keywords:** S-scheme charge transfer route,  $\text{Ag}_3\text{PO}_4/\text{C}_3\text{N}_4$ ,  $\text{Cr(VI)}$  reduction,  $\text{O}_2$  production, photocatalysis



## INTRODUCTION

Environmental pollution by heavy metals has become a great concern because of their toxic effects on plants, animals and human being. Among the numerous heavy metal ions, hexavalent chromium ( $\text{Cr(VI)}$ ) is a major critical contaminant in drinking water source because of its highly toxic, cancerogenic and mobile characteristics.<sup>[1-3]</sup> The reduction of  $\text{Cr(VI)}$  into  $\text{Cr(III)}$  has been applied to treat  $\text{Cr(VI)}$ -bearing wastewaters due to that  $\text{Cr(III)}$  is nontoxic with low solubility and mobility. Photocatalytic reduction as one of the promising strategies has drawn wide attention due to its high efficiency and environment friendly for removing  $\text{Cr(VI)}$ .<sup>[4-6]</sup> During photocatalytic  $\text{Cr(VI)}$  reduction in water, the photogenerated electrons were used to drive the reduction reaction, leaving the holes being consumed by sacrifice agents. Such a reductive half-reaction resulted in lower solar light conversion efficiency. Once suitable oxidative half-reaction was designed in the  $\text{Cr(VI)}$  reduction reaction system, the utilization of photons should be improved accompanied by the generation of useful products. Water oxidation is a typical oxidation reaction which could take advantage of the photogenerated holes.<sup>[7-10]</sup> Generally, the multi-electron process of water oxidation leads to slow kinetics which limits the  $\text{O}_2$  generation efficiency. Therefore, the combination of photocatalytic  $\text{O}_2$  generation with  $\text{Cr(VI)}$  reduction will not only accelerate the charge separation but also promote the quantum efficiency of the photocatalysts.

$\text{Ag}_3\text{PO}_4$  as an ideal semiconductor photocatalyst has demonstrated excellent performance in oxygen production and  $\text{Cr(VI)}$  removal. Liu et al prepared porous  $\text{Ag}/\text{Ag}_3\text{PO}_4/\text{GO}$  microspheres with a high reduction performance of hexavalent chromium after

30 h of continuous light irradiation.<sup>[11]</sup> Megala et al constructed a double direct Z-type photocatalyst  $\text{NiAl LDH}/\text{g-C}_3\text{N}_4/\text{Ag}_3\text{PO}_4$  to achieve improved performance of overall water splitting compared to the  $\text{NiAl LDH}/\text{g-C}_3\text{N}_4$  binary photocatalyst.<sup>[12]</sup> All such work indicated that  $\text{Ag}_3\text{PO}_4$ -based composites can serve as the potential photocatalysts in  $\text{O}_2$  production or  $\text{Cr(VI)}$  removal. However, there are few relevant reports on  $\text{Ag}_3\text{PO}_4$ -based photocatalysts for simultaneously realizing  $\text{Cr(VI)}$  reduction and water oxidation. Recently, S-scheme heterojunctions have achieved a success in photocatalysis because of their strong redox ability and unique charge carrier transfer efficiency.<sup>[13-16]</sup> Considering the advantages of S-scheme heterojunction, constructing  $\text{Ag}_3\text{PO}_4$ -based S-scheme heterojunction is a promising strategy to make full use of photogenerated electron/hole and realize simultaneously photocatalytic production of oxygen and  $\text{Cr(VI)}$  reduction. Graphitic carbon nitride ( $\text{g-C}_3\text{N}_4$ ), a stable and inexpensive metal-free polymeric semiconductor, can couple with  $\text{Ag}_3\text{PO}_4$  to construct an S-scheme heterojunction due to their matched energy band structure.<sup>[17-20]</sup> In addition,  $\text{C}_3\text{N}_4$  hollow spheres affording large specific surface areas and abundant reactive sites have been studied extensively. Zhang et al. prepared a porous hollow spherical  $\text{g-C}_3\text{N}_4$  catalyst decorated with single Cu atoms for selective oxidation of benzene to phenol.<sup>[21]</sup> Combining  $\text{C}_3\text{N}_4$  hollow spheres with  $\text{Ag}_3\text{PO}_4$  to construct an S-scheme heterojunction demonstrates great potential of simultaneous  $\text{Cr(VI)}$  reduction and oxygen production.

In this paper,  $\text{Ag}_3\text{PO}_4$  was coupled with hollow spherical  $\text{C}_3\text{N}_4$  to construct an S-scheme heterojunction by in situ precipitation method. The  $\text{Ag}_3\text{PO}_4/\text{C}_3\text{N}_4$  S-scheme heterojunction can realize the reduction of  $\text{Cr(VI)}$  to be  $\text{Cr(III)}$  and oxidation of water to

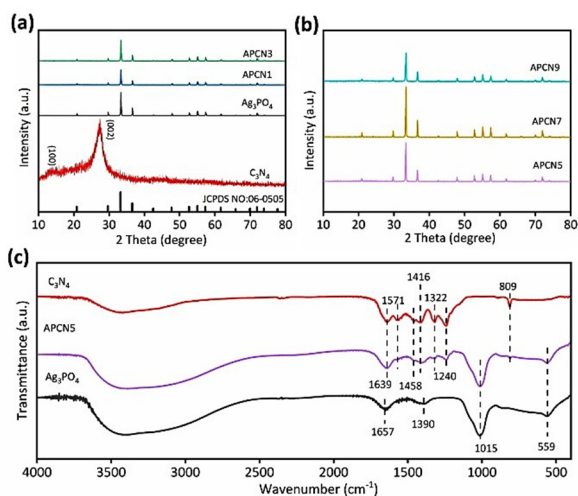


**Figure 1.** (a, b) XRD patterns of  $\text{Ag}_3\text{PO}_4$ ,  $\text{C}_3\text{N}_4$  and  $\text{Ag}_3\text{PO}_4/\text{C}_3\text{N}_4$  composites. (c) FTIR spectra of  $\text{Ag}_3\text{PO}_4$ ,  $\text{C}_3\text{N}_4$  and APCN5 nanocomposites.

produce oxygen in one reaction system. As a result, the optimized composite afforded high oxygen evolution of  $803.31 \mu\text{mol}\cdot\text{g}^{-1}\cdot\text{h}^{-1}$  and Cr(VI) conversion of 87.9% under visible light. The elemental valence and electron transfer route in  $\text{Ag}_3\text{PO}_4/\text{C}_3\text{N}_4$  have been studied by XPS and ESR spectra. The possible reaction mechanism of the simultaneous reduction Cr(VI) and oxygen production over  $\text{Ag}_3\text{PO}_4/\text{C}_3\text{N}_4$  S-scheme heterojunction was systematically studied.

## RESULTS AND DISCUSSION

XRD as well as FTIR was performed to analyze the crystal structure and constitution of the catalysts. Figure 1a displays the XRD patterns of  $\text{C}_3\text{N}_4$ ,  $\text{Ag}_3\text{PO}_4$  and  $\text{Ag}_3\text{PO}_4/\text{C}_3\text{N}_4$  composites. The characteristic peaks of  $\text{C}_3\text{N}_4$  located at  $27.3^\circ$  and  $13.1^\circ$  were attributed to the (002) and (100) faces of  $\text{C}_3\text{N}_4$ , which is in agreement with the reported literature.<sup>[22,23]</sup> The diffraction peaks of pure  $\text{Ag}_3\text{PO}_4$  also agreed with the standard PDF card for silver phosphate (JCPDS No: 06-0505).<sup>[24]</sup> For composite samples, only the characteristic peaks of  $\text{Ag}_3\text{PO}_4$  were observed since the mass content of  $\text{C}_3\text{N}_4$  was much lower than that of  $\text{Ag}_3\text{PO}_4$ .<sup>[25]</sup> However, the FTIR spectrum of APCN5 showed both the characteristic peaks of  $\text{Ag}_3\text{PO}_4$  and  $\text{C}_3\text{N}_4$  samples in Figure 1c. The signals at 1015 and  $559 \text{ cm}^{-1}$  were assigned to the stretching vibrations of the P-O bond in  $\text{PO}_4^{3-}$ . The peaks at 1657 and  $1390 \text{ cm}^{-1}$  were due to the stretching and bending of H-O bond in water. The characteristic peaks at 1240–1639  $\text{cm}^{-1}$  were the stretching vibrations of the CN heterocycle.<sup>[26]</sup> The peak at  $809 \text{ cm}^{-1}$  originated in the breathing vibration of the triazine unit.

The morphology of  $\text{Ag}_3\text{PO}_4$ ,  $\text{C}_3\text{N}_4$  and the  $\text{Ag}_3\text{PO}_4/\text{C}_3\text{N}_4$  composites was also investigated using the scanning electron microscopy (SEM).  $\text{Ag}_3\text{PO}_4$  is composed of irregular agglomerate grains (Figure 2a and b) with size of 300 nm.  $\text{C}_3\text{N}_4$  sample features the regular hollow sphere structure with the average diameter of 3–4  $\mu\text{m}$ . In  $\text{Ag}_3\text{PO}_4/\text{C}_3\text{N}_4$ , the  $\text{C}_3\text{N}_4$  hollow spheres could be preserved while  $\text{Ag}_3\text{PO}_4$  particles are dispersed on the surface of  $\text{C}_3\text{N}_4$  hollow spheres. As shown in the EDS mapping, it is clear that Ag, P, O, C and N elements homogeneously distributed in the

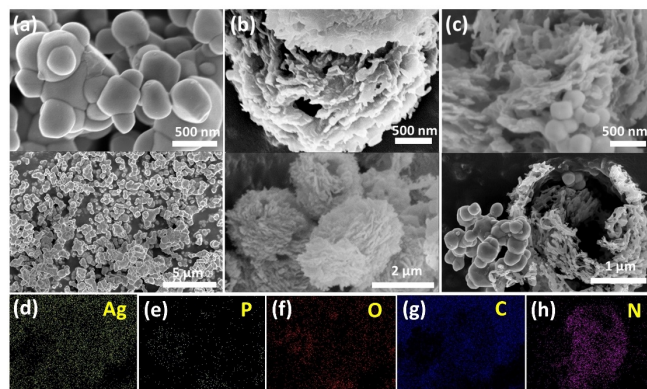


**Figure 2.** SEM pictures of  $\text{Ag}_3\text{PO}_4$  (a),  $\text{C}_3\text{N}_4$  (b), APCN5 (c) and corresponding elemental mapping images of Ag (d), P (e), O (f), C (g), N (h) elements in APCN5.

$\text{Ag}_3\text{PO}_4/\text{C}_3\text{N}_4$  composite.

XPS spectra were tested for studying the chemical composition. In the survey spectrum (Figure 3a), Ag, P, O, C and N were detected, which is consisted with the FTIR results. In Figure 3b, the bands at 367.74 and 373.74 eV can be referred to  $\text{Ag } 3d_{5/2}$  and  $\text{Ag } 3d_{3/2}$  in  $\text{Ag}_3\text{PO}_4$ .<sup>[27–29]</sup> Figure 3c shows that the P 2p peak at 132.68 eV belongs to the signal of  $\text{P}^{5+}$  in  $\text{Ag}_3\text{PO}_4$ . The O 1s spectrum (Figure 3d) depicts two different peaks at 530.41 and 532.20 eV, corresponding to the lattice oxygen and surface oxygen of  $\text{Ag}_3\text{PO}_4$ , respectively. Figure 3e shows the C 1s spectrum and the two bands located at 284.55 and 287.96 eV attributed to the  $\text{sp}^2$  C-C and N-C=N bonds of  $\text{C}_3\text{N}_4$  sample, respectively.<sup>[30]</sup> The peak

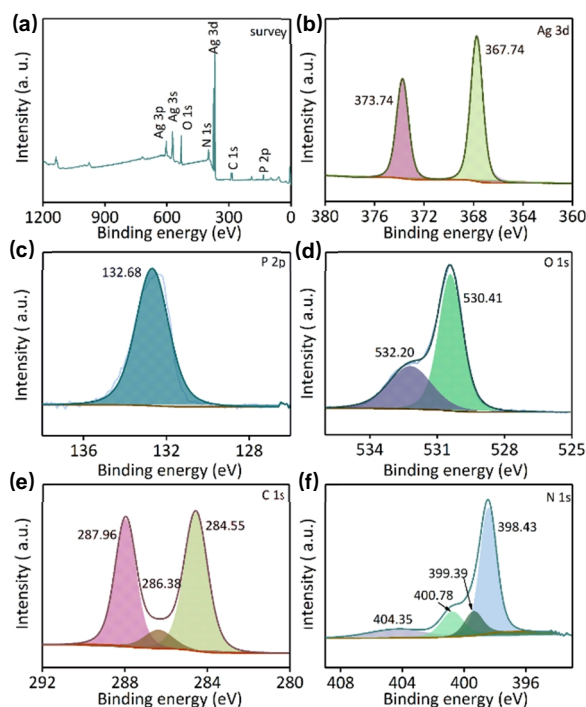


**Figure 3.** (a) XPS survey spectrum of the APCN5 composite. (b–f) High-resolution XPS spectrum of Ag 3d, P 2p, O 1s, C 1s and N 1s for the APCN5 sample.

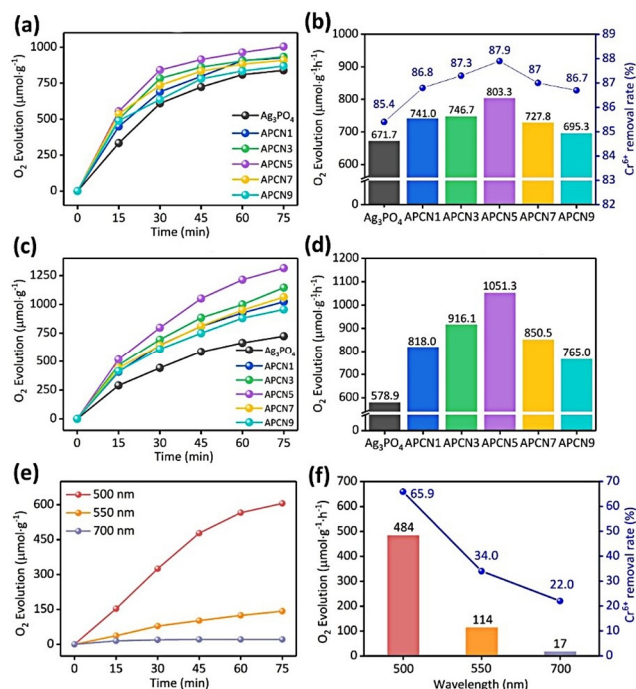


**Figure 4.** (a, b) Photocatalytic activities for O<sub>2</sub> generation coupled with Cr(VI) reduction of different samples. (c, d) Photocatalytic O<sub>2</sub> production activity with AgNO<sub>3</sub> as the sacrificial agent. (e, f) Photocatalytic activities for O<sub>2</sub> generation coupled with Cr(VI) reduction of APCN5 composites at different wavelengths.

at 286.38 eV appears to be the C=N bond of C<sub>3</sub>N<sub>4</sub> sample. The N 1s spectrum displays four peaks at 398.43, 399.39, 400.78 and 404.35 eV which belong to the pyridinic N, pyrrolic N, graphitic N and N<sub>2</sub>, respectively (Figure 3f).

Photocatalytic activities of Ag<sub>3</sub>PO<sub>4</sub>, C<sub>3</sub>N<sub>4</sub> and Ag<sub>3</sub>PO<sub>4</sub>/C<sub>3</sub>N<sub>4</sub> composites were evaluated by photocatalytic O<sub>2</sub> generation coupled with Cr(VI) reduction. As displayed in Figure 4a and b, when potassium dichromate is used as a Cr(IV) source, Ag<sub>3</sub>PO<sub>4</sub>/C<sub>3</sub>N<sub>4</sub> sphere composites exhibit a higher photocatalytic oxygen production performance than the pure Ag<sub>3</sub>PO<sub>4</sub> sample. The highest O<sub>2</sub> production is up to 803.31 μmol·h<sup>-1</sup>·g<sup>-1</sup> for APCN5. At the same time, the Cr(VI) reduction yield for APCN5 could get to 87.9% after 75 min light irradiation. Under the visible-light irradiation, the Cr(VI) reduction efficiency of the as-prepared photocatalysts follows the order of Ag<sub>3</sub>PO<sub>4</sub> < APCN9 < APCN1 < APCN7 < APCN5, which is consistent with that in the photocatalytic OER results. As shown in Figure S1, only 66.9% Cr(VI) conversion was obtained in the single Cr(VI) reduction reaction for APCN5 sample. When the sacrificial agent is replaced by AgNO<sub>3</sub>, the average photocatalytic O<sub>2</sub> evolution rates over Ag<sub>3</sub>PO<sub>4</sub>/C<sub>3</sub>N<sub>4</sub> composites are found to be 817.99, 916.05, 1051.33, 850.5 and 765.03 μmol·g<sup>-1</sup>·h<sup>-1</sup> for APCN1, APCN3, APCN5, APCN7 and APCN9, respectively. Obviously, with increasing the C<sub>3</sub>N<sub>4</sub> sphere mass ratio, the O<sub>2</sub> evolution activity increases greatly and then decreases gradually. The APCN5 affords the highest O<sub>2</sub> generation of 1051.33 μmol·g<sup>-1</sup>·h<sup>-1</sup>, which is 1.8 times of Ag<sub>3</sub>PO<sub>4</sub> (Figure 4c and d). As shown in Figure 4e and f, photocatalytic synchronous reduction of Cr(VI) and oxygen evolution with the optimal APCN5 sample at different wave-

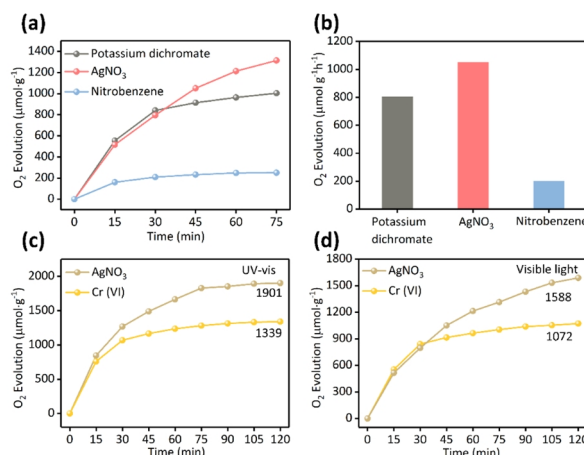


**Figure 5.** (a, b) Photocatalytic oxygen production of APCN5 with different sacrificial agents. The reactivity of oxygen production of the APCN5 composite under UV-vis (c) and visible light (d) excitation with different sacrificial agents.

lengths of 500, 550 and 700 nm were performed. The oxygen production at 500 nm reaches 484 μmol·g<sup>-1</sup>·h<sup>-1</sup> at 75 min and the conversion rate of Cr(VI) is 65.9%, while the oxygen production at 550 nm is 114 μmol·g<sup>-1</sup>·h<sup>-1</sup> and the conversion rate of Cr(VI) is 34.0%. The apparent quantum efficiency (AQY) of APCN5 is 5.5%, 14.8%, 1.8%, 0.8% and 0.05% at 365, 420, 500, 550, and 700 nm, respectively (Figure S2). All these results confirmed that the APCN5 could afford higher O<sub>2</sub> generation and Cr(VI) reduction activity than the reported photocatalysts listed in Table S1 and S2.

Different sacrificial agents were tested in the photocatalytic OER reaction. When potassium dichromate and nitrobenzene were used as electron-trapping sacrificial agents (Figure 5a and b), the APCN5 demonstrates lower photocatalytic OER activity (809.1 and 199.2 μmol·g<sup>-1</sup>·h<sup>-1</sup>) than AgNO<sub>3</sub> (1069.5 μmol·g<sup>-1</sup>·h<sup>-1</sup>). This indicates that AgNO<sub>3</sub> has the significant electron-trapping ability. As shown in Figure 5c and d, even after 120 min UV-visible and visible light irradiation with AgNO<sub>3</sub> as the sacrificial agent, APCN5 reaches 1901 and 1339 μmol g<sup>-1</sup> O<sub>2</sub> production, respectively. When Cr(VI) was used as the sacrificial agent, the oxygen production is 1588 and 1072 μmol g<sup>-1</sup>, and the conversion rate of Cr(VI) is 92.1% and 89.7%, respectively. These results revealed that the Ag<sub>3</sub>PO<sub>4</sub>/C<sub>3</sub>N<sub>4</sub> composite showed good photo-stability under UV-visible and visible light irradiation. The morphology of Ag<sub>3</sub>PO<sub>4</sub> and C<sub>3</sub>N<sub>4</sub> spheres of the composite could maintain their initial morphology before and after photocatalytic reaction (Figure S3), confirming their good stability.

To investigate the effect of C<sub>3</sub>N<sub>4</sub> morphologies on the photocatalytic performance, the Ag<sub>3</sub>PO<sub>4</sub>/C<sub>3</sub>N<sub>4</sub> composites with C<sub>3</sub>N<sub>4</sub> tube, C<sub>3</sub>N<sub>4</sub> bulk and C<sub>3</sub>N<sub>4</sub> sheets were synthesized. As shown in Figure 6a-c, the SEM images confirm the successful synthesis of Ag<sub>3</sub>PO<sub>4</sub>/C<sub>3</sub>N<sub>4</sub> tube, Ag<sub>3</sub>PO<sub>4</sub>/C<sub>3</sub>N<sub>4</sub> sheet and Ag<sub>3</sub>PO<sub>4</sub>/C<sub>3</sub>N<sub>4</sub> bulk composites. The corresponding BET specific surface area is shown in Table S3. The C<sub>3</sub>N<sub>4</sub> hollow sphere has the largest specific surface area (1617 m<sup>2</sup>/kg) than other morphologies (493.8, 479.3 and 507.3 m<sup>2</sup>/kg for C<sub>3</sub>N<sub>4</sub> tube, C<sub>3</sub>N<sub>4</sub> bulk and C<sub>3</sub>N<sub>4</sub> sheets, respectively). The photocatalytic O<sub>2</sub> evolution efficiency of these



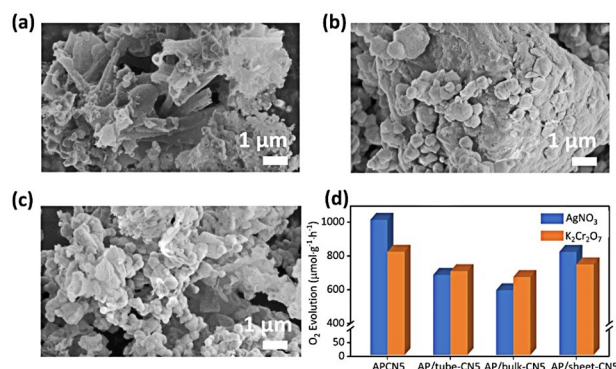


**Figure 6.** SEM images of Ag<sub>3</sub>PO<sub>4</sub>/C<sub>3</sub>N<sub>4</sub> tube (a), Ag<sub>3</sub>PO<sub>4</sub>/C<sub>3</sub>N<sub>4</sub> bulk (b) and Ag<sub>3</sub>PO<sub>4</sub>/C<sub>3</sub>N<sub>4</sub> sheet (c) composites. Photocatalytic activity of different samples (d).

samples follows the order: APCN5 > Ag<sub>3</sub>PO<sub>4</sub>/C<sub>3</sub>N<sub>4</sub> sheet composite > Ag<sub>3</sub>PO<sub>4</sub>/C<sub>3</sub>N<sub>4</sub> tube composite > Ag<sub>3</sub>PO<sub>4</sub>/C<sub>3</sub>N<sub>4</sub> bulk composite, indicating the superiority of hollow sphere structure of C<sub>3</sub>N<sub>4</sub> as the reduction semiconductor in the S-scheme heterojunction (Figure 6d).

To reveal the reactive species and understand the reaction mechanism, different kinds of trapping agents such as 1,4-benzoquinone (BQ), 1-butanol (NBA) and ethylenediaminetetraacetic acid disodium salt (EDTA-2Na) were applied as the scavenger to catch the superoxide radical ( $\cdot\text{O}_2^-$ ), hydroxyl radical ( $\cdot\text{OH}$ ) and hole ( $\text{h}^+$ ),<sup>[31–34]</sup> respectively. As listed in Figure 7a, the O<sub>2</sub> evolution efficiency of APCN5 declined in the presence of EDTA-2Na, BQ and NBA, suggesting that  $\text{h}^+$ ,  $\cdot\text{O}_2^-$  and OH all played important roles in the photocatalytic O<sub>2</sub> evolution. The Cr(VI) reduction was almost inhibited with the addition of BQ (Figure 7b), which verified that the  $\cdot\text{O}_2^-$  also has a positive effect on the reduction of Cr(VI). The addition of NBA and EDTA-2Na resulted in decreased reactivity in Cr(VI) reduction, indicating that  $\cdot\text{OH}$  and  $\text{h}^+$  are not the main active species during Cr(VI) reduction.

The charge separation and migration efficiency were also investigated by the photocurrent response, PL spectra, time-resolved PL (TRPL) decay spectra and the EIS Nyquist plots of the samples.<sup>[35–39]</sup> As can be seen in the photocurrent spectra in Figure 8a, the photocurrent intensity of APCN5 is higher than that of Ag<sub>3</sub>PO<sub>4</sub> and C<sub>3</sub>N<sub>4</sub>, illustrating the boosted charge separation in the composite. As shown in Figure 8b, pure C<sub>3</sub>N<sub>4</sub> spheres show stronger PL intensity than APCN5, which indicates low recombination rate of photogenerated carriers in APCN5 owing to the formation of close contact interface. The fluorescence lifetime of

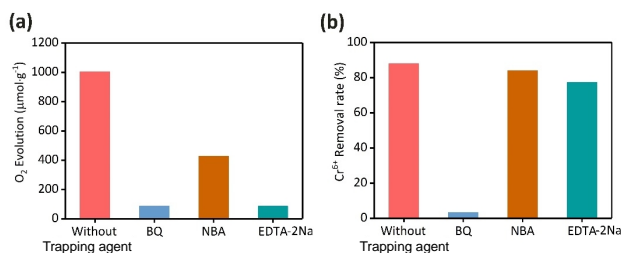


**Figure 7.** Trapping experiments for photocatalytic O<sub>2</sub> generation coupled with Cr(VI) reduction over APCN5.

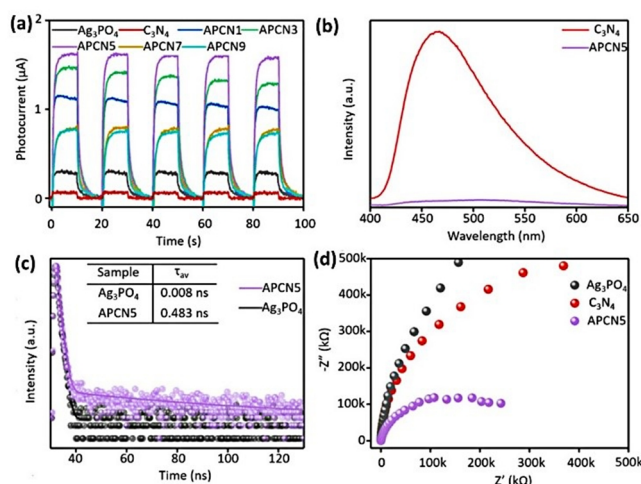


**Figure 8.** Transient photocurrent responses (a), PL spectra (b), Time-resolved PL decay spectra (c) and the EIS Nyquist plots (d) of C<sub>3</sub>N<sub>4</sub> spheres, Ag<sub>3</sub>PO<sub>4</sub> and APCN5 nanocomposites.

Ag<sub>3</sub>PO<sub>4</sub> and APCN5 is 0.008 and 0.483 ns, respectively (Figure 8c). The prolonged fluorescence lifetime of APCN5 implies enhanced separation of photogenerated charge carriers. The EIS plots show that the arc radius of APCN5 is smaller than that of Ag<sub>3</sub>PO<sub>4</sub> and C<sub>3</sub>N<sub>4</sub>, which improved charge separation and migration efficiency in the composite.

Figure 9 depicts the UV-vis DRS spectra of as-obtained samples. In comparison with pure Ag<sub>3</sub>PO<sub>4</sub> and C<sub>3</sub>N<sub>4</sub> spheres, the APCN composites show slightly red-shifted absorption in the visible light range with a light absorption threshold wavelength at 580 nm (Figure 9a). The band gaps  $E_g$  of Ag<sub>3</sub>PO<sub>4</sub> and C<sub>3</sub>N<sub>4</sub> spheres are 2.15 and 2.36 eV, respectively according to the reported calculation formula.<sup>[40–42]</sup> The positive slopes in the Mott-Schottky plots present n-type characteristic of Ag<sub>3</sub>PO<sub>4</sub> and C<sub>3</sub>N<sub>4</sub>. The flat-band potentials ( $E_{\text{FB}}$ ) of Ag<sub>3</sub>PO<sub>4</sub> and C<sub>3</sub>N<sub>4</sub> are about -0.38 and -1.02 eV (vs. Ag/AgCl), respectively. According to the Nernst equation, the  $E_{\text{CB}}$  values of Ag<sub>3</sub>PO<sub>4</sub> and C<sub>3</sub>N<sub>4</sub> are reckoned to be 0.21 and -0.42 eV,<sup>[43–46]</sup> respectively (Figure 9d).

The work functions of C<sub>3</sub>N<sub>4</sub> and Ag<sub>3</sub>PO<sub>4</sub> are further calculated,

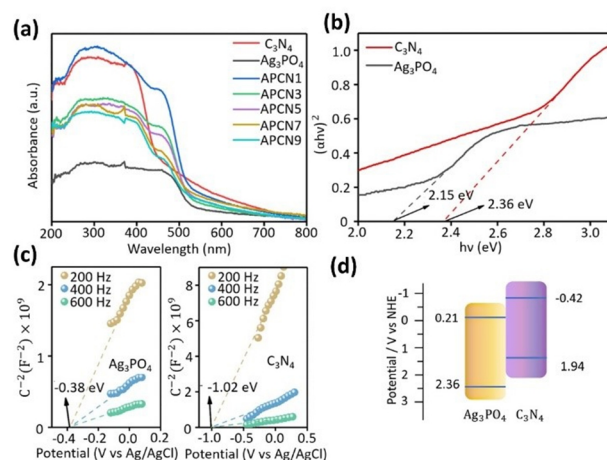
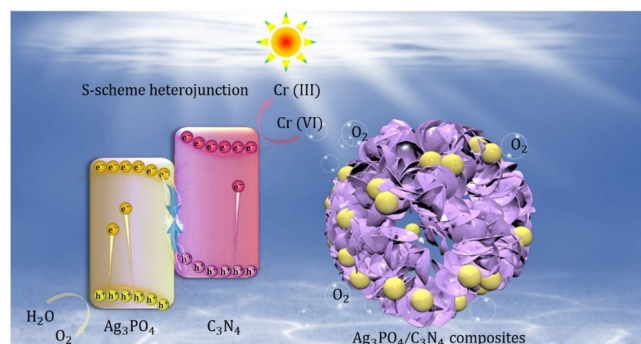


**Figure 9.** UV-Vis DRS (a), band gap energies (b), Mott-Schottky (M-S) plots (c) and energy band structure (d) of pure Ag<sub>3</sub>PO<sub>4</sub> and C<sub>3</sub>N<sub>4</sub> spheres.

and the values of g-C<sub>3</sub>N<sub>4</sub> and Ag<sub>3</sub>PO<sub>4</sub> are 4.60 and 4.75 eV, respectively (Figure 10 a and b), indicating that the electrons will migrate from C<sub>3</sub>N<sub>4</sub> to Ag<sub>3</sub>PO<sub>4</sub> to form an internal electric field (IEF) from C<sub>3</sub>N<sub>4</sub> to Ag<sub>3</sub>PO<sub>4</sub>.<sup>[47]</sup> IEF can work as a driving force for the migration of the photogenerated carriers. As a result, the energy band edges of C<sub>3</sub>N<sub>4</sub> and Ag<sub>3</sub>PO<sub>4</sub> bent upward and downward, respectively. EPR spectra were also investigated to study the photogenerated charge migration direction. As shown in the EPR spectra, the observed quartet peaks in Figure 10c and 10d are assigned to ·O<sub>2</sub><sup>-</sup> and ·OH, respectively.<sup>[48-52]</sup> Since the CB edge of Ag<sub>3</sub>PO<sub>4</sub> is more positive than that of O<sub>2</sub>/·O<sub>2</sub><sup>-</sup> (-0.33 V vs. NHE) while the CB edge of C<sub>3</sub>N<sub>4</sub> is more negative than -0.33 V, the ·O<sub>2</sub><sup>-</sup> cannot be generated in the presence of Ag<sub>3</sub>PO<sub>4</sub>. In addition, the oxidation potential of H<sub>2</sub>O/·OH (1.99 V vs. NHE) is more negative but more positive than that of the VB edge of Ag<sub>3</sub>PO<sub>4</sub> and C<sub>3</sub>N<sub>4</sub>, respectively. ·OH cannot be generated under the circumstance of bare C<sub>3</sub>N<sub>4</sub>. However, after the combination of C<sub>3</sub>N<sub>4</sub> spheres with Ag<sub>3</sub>PO<sub>4</sub>, the composite could generate both ·O<sub>2</sub><sup>-</sup> and ·OH, which confirms the S-scheme in the Ag<sub>3</sub>PO<sub>4</sub>/C<sub>3</sub>N<sub>4</sub> sphere composite. The photogenerated e<sup>-</sup> on the CB of Ag<sub>3</sub>PO<sub>4</sub> reacts with h<sup>+</sup> on the VB of C<sub>3</sub>N<sub>4</sub> while the e<sup>-</sup> on that of C<sub>3</sub>N<sub>4</sub> and the h<sup>+</sup> on the VB of Ag<sub>3</sub>PO<sub>4</sub> are preserved for offering the stronger redox ability and fast e<sup>-</sup>-h<sup>+</sup> separation.

According to the above results, the simultaneous oxygen production and Cr(VI) reduction reaction mechanism were discussed over the Ag<sub>3</sub>PO<sub>4</sub>/C<sub>3</sub>N<sub>4</sub> sphere composite. As shown in Scheme 1, the Ag<sub>3</sub>PO<sub>4</sub> and C<sub>3</sub>N<sub>4</sub> spheres were excited by light. The photo-generated e<sup>-</sup> of Ag<sub>3</sub>PO<sub>4</sub> recombined with the h<sup>+</sup> of C<sub>3</sub>N<sub>4</sub> spheres at the intimate interface driven by the formed IEF. At the same



**Scheme 1.** Schematic illustration of simultaneous production of oxygen and reduction of Cr(VI) over the Ag<sub>3</sub>PO<sub>4</sub>/C<sub>3</sub>N<sub>4</sub> spheres S-scheme heterojunction under visible-light irradiation.

time, the e<sup>-</sup> and h<sup>+</sup> with stronger redox ability at the CB of Ag<sub>3</sub>PO<sub>4</sub> and the VB of C<sub>3</sub>N<sub>4</sub> spheres tended to take part in the reduction of Cr(VI) and production of oxygen, respectively. In detail, the e<sup>-</sup> and h<sup>+</sup> accumulated in the CB of C<sub>3</sub>N<sub>4</sub> spheres and VB of Ag<sub>3</sub>PO<sub>4</sub> reacted respectively with Cr(VI) and H<sub>2</sub>O to generate Cr(III) and O<sub>2</sub>.

## CONCLUSION

Novel S-scheme heterojunction of Ag<sub>3</sub>PO<sub>4</sub>/C<sub>3</sub>N<sub>4</sub> sphere composite was designed and fabricated via an in-situ precipitation method. The results revealed that APCN5 exhibits high-efficiency for the photocatalytic removal of Cr(VI) and oxygen production. Under optimal conditions, APCN5 could give an 87.9% conversion of Cr(VI) into Cr(III) and an O<sub>2</sub> production of 803.31 μmol·g<sup>-1</sup>·h<sup>-1</sup>, respectively. The improved activity is due to the following reasons: (i) the Ag<sub>3</sub>PO<sub>4</sub>/C<sub>3</sub>N<sub>4</sub> sphere composite provided abundant reactive sites; (ii) the S-scheme transfer pathway contributed to the efficient separation of charges and strong redox capability. This research may provide a new strategy for developing an effective heterostructure toward photocatalytic O<sub>2</sub> production as well as the wastewater purification.

## EXPERIMENTAL

### Photocatalyst Synthesis

**C<sub>3</sub>N<sub>4</sub> Spheres.** 0.5 g of melamine was added into 20 mL dimethyl sulfoxide (DMSO). After ultrasonic dispersion, the obtained solution is recorded as liquid A. Then, 0.51 g of melamine was dispersed in 10 mL of DMSO. After ultrasonication, the obtained solution is recorded as liquid B. The obtained solutions A and B were mixed under stirring for 10 min and the product was washed with anhydrous ethanol and deionized water for 2 times, respectively. After centrifuging and drying, the white powder was obtained. Then, the white powder was heated at 550 °C (2.5 °C/min) under N<sub>2</sub> atmosphere for 4 h to obtain the yellow g-C<sub>3</sub>N<sub>4</sub> spheres.<sup>[53]</sup>

**g-C<sub>3</sub>N<sub>4</sub> Sheets.** 15 g of urea was treated at 550 °C in a muffle furnace for 4 h (2 °C/min) to obtain the light-yellow g-C<sub>3</sub>N<sub>4</sub> sheets powder.

**C<sub>3</sub>N<sub>4</sub> Tubes.** 1.5 g of urea and 0.4 g of melamine were mixed and fully ground for 30 min under N<sub>2</sub> atmosphere. Then, the mixture

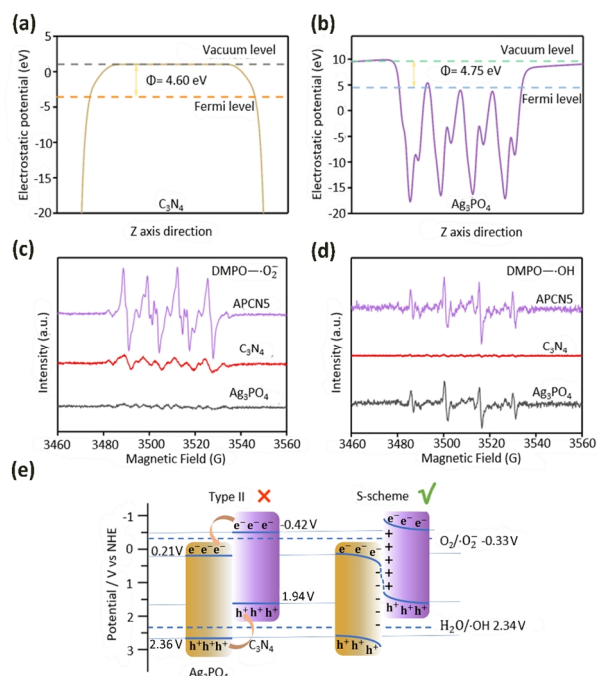


**Figure 10.** (a, b) The calculated work functions of Ag<sub>3</sub>PO<sub>4</sub> and C<sub>3</sub>N<sub>4</sub>. (c, d) EPR spectra of DMPO·O<sub>2</sub><sup>-</sup> and DMPO·OH signals over Ag<sub>3</sub>PO<sub>4</sub>, C<sub>3</sub>N<sub>4</sub>, and APCN5 composites, respectively. (e) Schematic diagram of photogenerated charges in the Ag<sub>3</sub>PO<sub>4</sub>/C<sub>3</sub>N<sub>4</sub> sphere composite.

was treated at 550 °C for 4 h (5 °C/min) to obtain the light-yellow C<sub>3</sub>N<sub>4</sub> tubes.

**C<sub>3</sub>N<sub>4</sub> Bulk.** 15 g of melamine was treated to 550 °C in a muffle furnace for 4 h (2 °C/min) to get light-yellow C<sub>3</sub>N<sub>4</sub> bulk.

**Ag<sub>3</sub>PO<sub>4</sub>/C<sub>3</sub>N<sub>4</sub> Sphere Composites.** Different contents of C<sub>3</sub>N<sub>4</sub> spheres (4, 12, 20, 28 and 36 mg, respectively) with 0.51 g of AgNO<sub>3</sub> were added into the mixed solution of 10 mL of N,N-dimethylformamide (DMF) and 10 mL deionized water under continuous ultrasonication. Afterwards, 0.1 M Na<sub>2</sub>HPO<sub>4</sub> solution was poured and stirred for 30 min. The precipitate was washed with anhydrous ethanol and water respectively, centrifuged and dried at 70 °C for 4 h, obtaining a yellow powder. The obtained products were named as APCN1, APCN3, APCN5, APCN7 and APCN9 (The mass ratios of C<sub>3</sub>N<sub>4</sub> spheres are 1%, 3%, 5%, 7% and 9%, respectively).

**Characterization.** The XRD pattern was used to analyze the structure of the sample with an X-ray diffractometer instrument (D8 Advance, Bruker, Germany) in the 2θ range from 10° to 80°. The micromorphology and the corresponding elemental composition of the samples were examined by SEM (JSM-7001F). The Fourier transform infrared spectra of the sample were carried out on a Nicolet 460 Fourier transform infrared spectrometer (FTIR, Nicolet 460, USA). UV-vis DRS spectra were performed on a Shimadzu UV-2600 spectrometer. The XPS spectra were performed on a Scienta R3000 spectrometer. The photocurrent density curves (I-T), electrochemical impedance spectroscopy (EIS) as well as Mott-Schottky curves for the sample were checked on the electrochemical workstation (CHI 660E, ChenHua Instruments, Shanghai) with three electrodes (Pt electrode, Ag/AgCl electrode and working electrode).<sup>[54]</sup> EPR analysis was performed on a Bruker A 300 instrument.

**Photocatalytic Tests.** The photocatalytic O<sub>2</sub> production was performed on an online gas chromatography system (Labsolar-6A, Perfect light) using a sealed air tight quartz reactor. The photocatalytic reactor contained 25 mg of samples and 50 mL of aqueous solution with 0.06 M AgNO<sub>3</sub> solution and 20 mg/L of K<sub>2</sub>Cr<sub>2</sub>O<sub>7</sub> solution (as the Cr source). The reaction system was irradiated for 75 min under a 300 W Xe lamp using a filter with λ ≥ 420 nm. The evolution rate of oxygen was measured by a gas chromatograph (GC-2014 Shimadzu). The concentration of Cr(VI) was analyzed by a UV-2600 spectrophotometer with its absorption wavelength to be at 356 nm.

## ACKNOWLEDGEMENTS

This work is supported by the National Natural Science Foundation of China (21975110, 21972058 and 22102064), and Prof. H. Tang gratefully acknowledges the financial support from Taishan Youth Scholar Program of Shandong Province.

## AUTHOR INFORMATION

Corresponding authors. Emails: huatang79@163.com, hujiechem@hotmail.com and qqliu@ujs.edu.cn

## AUTHOR CONTRIBUTION

<sup>†</sup> These authors contribute equally to this work

## COMPETING INTERESTS

The authors declare no competing interests.

## ADDITIONAL INFORMATION

Supplementary information is available for this paper at <http://manu30.magtech.com.cn/jghx/EN/10.14102/j.cnki.0254-5861.2022-0062>

For submission: <https://mc03.manuscriptcentral.com/cjsc>

## REFERENCES

- (1) Wang, C.; Wang, K. W.; Feng, Y. B.; Li, C.; Zhou, X. Y.; Gan, L. Y.; Feng, Y. J.; Zhou, H. J.; Zhang, B.; Qu, X. L.; Li, H.; Li, J. Y.; Li, A.; Sun, Y. Y.; Zhang, S. B.; Yang, G.; Guo, Y. Z.; Yang, S. Z.; Zhou, T. H.; Dong, F.; Zheng, K.; Wang, L. H.; Huang, J.; Zhang, Z.; Han, X. D. Co and Pt dual single atoms with oxygen coordinated Co-O-Pt dimer sites for ultrahigh photocatalytic hydrogen evolution efficiency. *Adv. Mater.* **2021**, 33, 2003327.
- (2) Wang, L. L.; Tang, G. G.; Liu, S.; Dong, H. L.; Liu, Q. Q.; Sun, J. F.; Tang, H. Interfacial active-site-rich 0D Co<sub>3</sub>O<sub>4</sub>/1D TiO<sub>2</sub> p-n heterojunction for enhanced photocatalytic hydrogen evolution. *Chem. Eng. J.* **2022**, 428, 131338.
- (3) Bie, C. B.; Yu, H. G.; Cheng, B.; Ho, W. K.; Fan, J. J.; Yu, J. G. Design, fabrication, and mechanism of nitrogen doped graphene based photocatalyst. *Adv. Mater.* **2021**, 33, 2003521.
- (4) Sun, J. L.; Hou, Y. P.; Yu, Z. B.; Tu, L. L.; Yan, Y. M.; Qin, S. M.; Chen, S.; Lan, D. Q.; Zhu, H. X.; Wang, H. F. Visible-light-driven Z-scheme Zn<sub>3</sub>In<sub>2</sub>Se<sub>8</sub>/AgBr photocatalyst for boosting simultaneous Cr(VI) reduction and metronidazole oxidation: kinetics, degradation pathways and mechanism. *J. Hazard. Mater.* **2021**, 419, 126543.
- (5) Chen, Z. L.; Luo, Y. Y.; Huang, C. X.; Shen, X. T. In situ assembly of ZnO/graphene oxide on synthetic molecular receptors: towards selective photoreduction of Cr(VI) via interfacial synergistic catalysis. *Chem. Eng. J.* **2021**, 414, 128914.
- (6) Liu, H. D.; Cheng, M.; Liu, Y.; Zhang, G. X.; Li, L.; Du, L.; Li, B.; Xiao, S.; Wang, G. F.; Yang, X. F. Modified UiO-66 as photocatalysts for boosting the carbon-neutral energy cycle and solving environmental remediation issues. *Coord. Chem. Rev.* **2022**, 458, 214428.
- (7) Wang, Y. N.; Huang, J. W.; Wang, L.; She, H. D.; Wang, Q. Z. Research progress of ferrite materials for photoelectrochemical water splitting. *Chin. J. Struct. Chem.* **2022**, 41, 2201054-2201068.
- (8) Li, D. S.; Liu, Y.; Yang, Y. T.; Tang, G. G.; Tang, H. Rational construction of Ag<sub>3</sub>PO<sub>4</sub>/WO<sub>3</sub> step-scheme heterojunction for enhanced solar-driven photocatalytic performance of O<sub>2</sub> evolution and pollutant degradation. *J. Colloid Interface Sci.* **2022**, 608, 2549-2559.
- (9) Meng, L.; Feng, L. G. NiSe<sub>2</sub>-CoSe<sub>2</sub> with a hybrid nanorods and nanoparticles structure for efficient oxygen evolution reaction. *Chin. J. Struct. Chem.* **2022**, 41, 2201019-2201024.
- (10) Dong, B. B.; Cui, J. Y.; Qi, Y.; Zhang, F. X. Nanostructure engineering and modulation of (oxy)nitrides for application in visible-light-driven water splitting. *Adv. Mater.* **2021**, 33, 2004697.
- (11) Liu, Y. X.; Yang, D. Z.; Xu, T.; Shi, Y. Z.; Song, L. N.; Yu, Z. Z. Continuous photocatalytic removal of chromium (VI) with structurally stable and porous Ag/Ag<sub>3</sub>PO<sub>4</sub>/reduced graphene oxide microspheres. *Chem. Eng. J.* **2020**, 379, 122200.
- (12) Megala, S.; Ravi, P.; Maadeswaran, P.; Navaneethan, M.; Ramesh, R.



The construction of a dual direct Z-scheme NiAl LDH/g-C<sub>3</sub>N<sub>4</sub>/Ag<sub>3</sub>PO<sub>4</sub> nanocomposite for enhanced photocatalytic oxygen and hydrogen evolution. *Nanoscale Adv.* **2021**, 7, 2075-2088.

(13) Liu, Q. Q.; He, X. D.; Tao, J. N.; Tang, H.; Liu, Z. Q. Oxygen vacancies induced plasmonic effect for realizing broad-spectrum-driven photocatalytic H<sub>2</sub> evolution over an S-scheme CdS/W<sub>18</sub>O<sub>49</sub> heterojunction. *Chem-NanoMat* **2020**, 7, 44-49.

(14) Zulfiqar, S.; Liu, S.; Rahman, N.; Tang, H.; Shah, S.; Yu, X. H.; Liu, Q. Q. Construction of S-scheme MnO<sub>2</sub>@CdS heterojunction with core-shell structure as H<sub>2</sub> production photocatalyst. *Rare Metals* **2021**, 40, 2381-2391.

(15) Tao, J. N.; Yu, X. H.; Liu, Q. Q.; Liu, G. W.; Tang, H. Internal electric field induced S-scheme heterojunction MoS<sub>2</sub>/CoAl LDH for enhanced photocatalytic hydrogen evolution. *J. Colloid Interface Sci.* **2021**, 585, 470-479.

(16) Zhang, L. Y.; Zhang, J. J.; Yu, H. G.; Yu, J. G. Emerging S-scheme photocatalyst. *Adv. Mater.* **2021**, 34, 2107668.

(17) Jia, X. X.; Zhao, J. W.; Lv, Y. G.; Fu, X. L.; Jian, Y. J.; Zhang, W. Q.; Wang, Y. Y.; Sun, H. M.; Wang, X. X.; Long, J. L.; Yang, P.; Gu, Q.; Gao, Z. W. Low-crystalline PdCu alloy on large-area ultrathin 2D carbon nitride nanosheets for efficient photocatalytic Suzuki coupling. *Appl. Catal., B-Environ.* **2022**, 300, 120756.

(18) Liu, Q. Q.; He, X. D.; Peng, J. J.; Yu, X. H.; Tang, H.; Zhang, J. Hot electron assisted S-scheme heterojunction of tungsten oxide/graphitic carbon nitride for broad spectrum photocatalytic H<sub>2</sub> generation. *Chin. J. Catal.* **2021**, 42, 1478-1487.

(19) Ren, M. L.; Ao, Y. H.; Wang, P. F.; Wang, C. Construction of silver/graphitic-C<sub>3</sub>N<sub>4</sub>/bismuth tantalate Z-scheme photocatalyst with enhanced visible-light-driven performance for sulfamethoxazole degradation. *Chem. Eng. J.* **2019**, 378, 122122.

(20) Che, H. N.; Gao, X.; Chen, J.; Hou, J.; Ao, Y. H.; Wang, P. F. Iodide-induced fragmentation of polymerized hydrophilic carbon nitride for high-performance quasi-homogeneous photocatalytic H<sub>2</sub>O<sub>2</sub> production. *Angew. Chem. Int. Ed.* **2021**, 60, 25546-25550.

(21) Wang, G. C.; Zhang, T.; Yu, W. W.; Si, R.; Liu, Y. F.; Zhao, Z. K. Modulating location of single copper atoms in polymeric carbon nitride for enhanced photoredox catalysis. *ACS Catal.* **2020**, 10, 5715-5722.

(22) Zhang, T.; Zhang, D.; Han, X. H.; Dong, T.; Guo, X. W.; Song, C. S.; Si, R.; Liu, W.; Liu, Y. F.; Zhao, Z. K. Preassembly strategy to single Cu-N<sub>3</sub> sites inlaid porous hollow carbonitride spheres for selective oxidation of benzene to phenol. *J. Am. Chem. Soc.* **2018**, 140, 16936-16940.

(23) Hong, X. Y.; Yu, X. H.; Wang, L. L.; Liu, Q. Q.; Sun, J. F.; Tang, H. Lattice-matched CoP/CoS<sub>2</sub> heterostructure cocatalyst to boost photocatalytic H<sub>2</sub> generation. *Inorg. Chem.* **2021**, 60, 12506-12516.

(24) Tang, H.; Xia, Z. H.; Chen, R.; Liu, Q. Q.; Zhou, T. H. Oxygen doped g-C<sub>3</sub>N<sub>4</sub> with nitrogen vacancy for enhanced photocatalytic hydrogen evolution. *Chem. Asian J.* **2020**, 15, 3456-3461.

(25) Wu, Y.; Chen, J.; Che, H.; Gao, X.; Ao, Y.; Wang, P. Boosting 2 e<sup>-</sup> oxygen reduction reaction in garland carbon nitride with carbon defects for high-efficient photocatalysis-self-Fenton degradation of 2,4-dichlorophenol. *Appl. Catal., B-Environ.* **2022**, 307, 121185.

(26) Wu, X. H.; Ma, H. Q.; Zhong, W.; Fan, J. J.; Yu, H. G. Porous crystalline g-C<sub>3</sub>N<sub>4</sub>: bifunctional NaHCO<sub>3</sub> template-mediated synthesis and improved photocatalytic H<sub>2</sub>-evolution rate. *Appl. Catal. B-Environ.* **2020**, 271, 118899.

(27) Lin, Y.; Yang, C. P.; Niu, Q. Y.; Luo, S. L. Interfacial charge transfer between silver phosphate and W<sub>2</sub>N<sub>3</sub> induced by nitrogen vacancies en-

hances removal of β-lactam antibiotics. *Adv. Funct. Mater.* **2021**, 32, 2108814.

(28) Prasad, C.; Tang, H.; Liu, Q. Q.; Bahadur, I.; Karlapudi, S.; Jiang, Y. J. A latest overview on photocatalytic application of g-C<sub>3</sub>N<sub>4</sub> based nanostructured materials for hydrogen production. *Int. J. Hydrogen Energy* **2020**, 45, 337-379.

(29) Yang, Z. F.; Xia, X. N.; Shao, L. H.; Wang, L. L.; Liu, Y. T. Efficient photocatalytic degradation of tetracycline under visible light by Z-scheme Ag<sub>3</sub>PO<sub>4</sub>/mixed-valence MIL-88A(Fe) heterojunctions: mechanism insight, degradation pathways and DFT calculation. *Chem. Eng. J.* **2021**, 410, 128454.

(30) Chang, H. B.; Liu, J. B.; Dong, Z.; Wang, D. D.; Xin, Y.; Jiang, Z. L.; Tang, S. S. Enhancement of photocatalytic degradation of polyvinyl chloride plastic with Fe<sub>2</sub>O<sub>3</sub> modified AgNbO<sub>3</sub> photocatalyst under visible-light irradiation. *Chin. J. Struct. Chem.* **2021**, 40, 1595-1603.

(31) Naciri, Y.; Hsini, A.; Bouziani, A.; Djellabi, R.; Ajmal, Z.; Laabd, M.; Navio, J. A.; Mills, A.; Bianchi, C. L.; Li, H.; Bakiz, B.; Albourine, A. Photocatalytic oxidation of pollutants in gas-phase via Ag<sub>3</sub>PO<sub>4</sub>-based semiconductor photocatalysts: recent progress, new trends, and future perspectives. *Crit. Rev. Environ. Sci. Technol.* **2021**, 2, 1-44.

(32) Liu, Q. Q.; Huang, J. X.; Wang, L. L.; Yu, X. H.; Sun, J. F.; Tang, H. Unraveling the roles of hot electrons and cocatalyst toward broad spectrum photocatalytic H<sub>2</sub> generation of g-C<sub>3</sub>N<sub>4</sub> nanotube. *Sol. RRL* **2021**, 5, 2000504.

(33) Chen, G. H.; Wang, H. J.; Dong, W. Y.; Huang, Y. X.; Zhao, Z. L.; Zeng, Y. X. Graphene dispersed and surface plasmon resonance-enhanced Ag<sub>3</sub>PO<sub>4</sub> (DSR-Ag<sub>3</sub>PO<sub>4</sub>) for visible light driven high-rate photodegradation of carbamazepine. *Chem. Eng. J.* **2021**, 405, 126850.

(34) Gao, D. D.; Zhong, W.; Liu, Y. P.; Yu, H. G.; Fan, J. J. Synergism of tellurium-rich structure and amorphization of NiTe<sub>1+x</sub> nanodots for efficient photocatalytic H<sub>2</sub> evolution. *Appl. Catal. B-Environ.* **2021**, 290, 120057.

(35) Deng, C. L.; Sun, C. F.; Wang, Z.; Tao, Y. W.; Chen, Y. L.; Lin, J. Q.; Luo, G. G.; Lin, B. Z.; Sun, D.; Zheng, L. S. A sodalite-type silver orthophosphate cluster in a globular silver nanocluster. *Angew. Chem., Int. Ed.* **2020**, 59, 12659-12663.

(36) Chen, R.; Chen, J.; Che, H.; Zhou, G.; Ao, Y.; Liu, B. Atomically dispersed main group magnesium on cadmium sulfide as the active site for promoting photocatalytic hydrogen evolution catalysis. *Chin. J. Struct. Chem.* **2022**, 41, 2201014-2201018.

(37) Xiong, Z.; Hou, Y. D.; Yuan, R. S.; Ding, Z. X.; Ong, W. J.; Wang, S. B. Hollow NiCo<sub>2</sub>S<sub>4</sub> nanospheres as a cocatalyst to support ZnIn<sub>2</sub>S<sub>4</sub> nanosheets for visible-light-driven hydrogen production. *Acta Phys.-Chim. Sin.* **2022**, 38, 2111021.

(38) Li, B.; Wei, F.; Su, B.; Guo, Z.; Ding, Z.; Yang, M. Q.; Wang, S. Mesoporous cobalt tungstate nanoparticles for efficient and stable visible-light-driven photocatalytic CO<sub>2</sub> reduction. *Mater. Today Energy* **2022**, 24, 100943.

(39) Lin, X. H.; Xie, Z. D.; Su, B.; Zheng, M.; Dai, W. X.; Hou, Y. D.; Ding, Z. X.; Lin, W.; Fang, Y. X.; Wang, S. B. Well-defined Co<sub>9</sub>S<sub>8</sub> cages enable the separation of photoexcited charges to promote visible-light CO<sub>2</sub> reduction. *Nanoscale* **2021**, 13, 18070-18076.

(40) Wang, R.; Yang, P.; Wang, S.; Wang, X. Distorted carbon nitride nanosheets with activated n→π\* transition and preferred textural properties for photocatalytic CO<sub>2</sub> reduction. *J. Catal.* **2021**, 402, 166-176.

(41) Li, B. F.; Wang, W. J.; Zhao, J. W.; Wang, Z. Y.; Su, B.; Hou, Y. D.; Ding, Z. X.; Ong, W. J.; Wang, S. B. All-solid-state direct Z-scheme Ni

TiO<sub>2</sub>/Cd<sub>0.5</sub>Zn<sub>0.5</sub>S heterostructures for photocatalytic hydrogen evolution with visible light. *J. Mater. Chem. A* **2021**, 9, 10270-10276.

(42) Ma, X.; Cheng, H. F. Facet-dependent photocatalytic H<sub>2</sub>O<sub>2</sub> production of single phase Ag<sub>3</sub>PO<sub>4</sub> and Z-scheme Ag/ZnFe<sub>2</sub>O<sub>4</sub>-Ag-Ag<sub>3</sub>PO<sub>4</sub> composites. *Chem. Eng. J.* **2022**, 429, 132373.

(43) Zhou, L.; Zhang, X.; Cai, M.; Cui, N. X.; Chen, G. F.; Zou, G. Y. New insights into the efficient charge transfer of the modified-TiO<sub>2</sub>/Ag<sub>3</sub>PO<sub>4</sub> composite for enhanced photocatalytic destruction of algal cells under visible light. *Appl. Catal., B-Environ.* **2022**, 302, 120868.

(44) Liu, Q. Q.; Huang, J. X.; Tang, H.; Yu, X. H.; Shen, J. Construction 0D TiO<sub>2</sub> nanoparticles/2D CoP nanosheets heterojunctions for enhanced photocatalytic H<sub>2</sub> evolution activity. *J. Mater. Sci. Technol.* **2020**, 56, 196-205.

(45) Shi, W. L.; Guo, F.; Yuan, S. L. In situ synthesis of Z-scheme Ag<sub>3</sub>PO<sub>4</sub>/CuBi<sub>2</sub>O<sub>4</sub> photocatalysts and enhanced photocatalytic performance for the degradation of tetracycline under visible light irradiation. *Appl. Catal., B-Environ.* **2017**, 209, 720-728.

(46) Han, S. T.; Li, B. F.; Huang, L. J.; Xi, H. L.; Ding, Z. X.; Long, J. J. Construction of ZnIn<sub>2</sub>S<sub>4</sub>-CdIn<sub>2</sub>S<sub>4</sub> microspheres for efficient photo-catalytic reduction of CO<sub>2</sub> with visible light. *Chin. J. Struct. Chem.* **2022**, 41, 2201007-2201013

(47) Wang, R.; Shen, J.; Zhang, W. J.; Liu, Q. Q.; Zhang, M. Y.; Zulficar; Tang, H. Build-in electric field induced step-scheme TiO<sub>2</sub>/W<sub>18</sub>O<sub>49</sub> heterojunction for enhanced photocatalytic activity under visible-light irradiation. *Ceram. Int.* **2020**, 46, 23-30.

(48) Xu, J.; Chen, J.; Ao, Y. H.; Wang, P. F. 0D/1D AgI/MoO<sub>3</sub> Z-scheme heterojunction photocatalyst: highly efficient visible-light-driven photocatalyst for sulfamethoxazole degradation. *Chin. Chem. Lett.* **2021**, 32, 3226-3230.

(49) Zhu, B. C.; Hong, X. Y.; Tang, L. Y.; Liu, Q. Q.; Tang, H. Enhanced photocatalytic CO<sub>2</sub> reduction over 2D/1D BiOBr<sub>0.5</sub>Cl<sub>0.5</sub>/WO<sub>3</sub> S-scheme heterostructure. *Acta Phys. -Chim. Sin.* **2022**, 38, 2111008.

(50) Wang, W. C.; Tao, Y.; Du, L. L.; Zhen, W.; Yan, Z. P.; Chan, W. K.; Lian, Z. C.; Zhu, R. X.; Philips, D. L.; Li, G. S. Femtosecond time-resolved spectroscopic observation of long-lived charge separation in bimetallic sulfide/g-C<sub>3</sub>N<sub>4</sub> for boosting photocatalytic H<sub>2</sub> evolution. *Appl. Catal., B-Environ.* **2021**, 282, 1195688.

(51) Wei, Y.; Chen, L. J.; Chen, H.; Cai, L. R.; Tan, G. P.; Qiu, Y. F.; Xiang, Q. J.; Chen, G.; Lau, T. C.; Robert, M. Highly efficient photocatalytic reduction of CO<sub>2</sub> to CO by in situ formation of a hybrid catalytic system based on molecular iron quaterpyridine covalently linked to carbon nitride. *Angew. Chem. Int. Ed.* **2022**, 61, e202116832.

(52) Peng, J. J.; Shen, J.; Yu, X. H.; Tang, H.; Zulficar; Liu, Q. Q. Construction of LSPR-enhanced 0D/2D CdS/MoO<sub>3-x</sub> S-scheme heterojunctions for visible-light-driven photocatalytic H<sub>2</sub> evolution. *Chin. J. Catal.* **2021**, 42, 87-96.

(53) Shen, R. C.; Lu, X. Y.; Zheng, Q. Q.; Chen, Q.; Ng, Y. H.; Zhang, P.; Li, X. Tracking S-scheme charge transfer pathways in Mo<sub>2</sub>C/CdS H<sub>2</sub>-evolution photocatalysts. *Sol. RRL.* **2021**, 5, 2100177.

(54) Zhang, X.; Ma, P. J.; Wang, C.; Gan, L. Y.; Chen, X. J.; Zhang, P.; Wang, Y.; Li, H.; Wang, L. H.; Zhou, X. Y.; Zheng, K. Unraveling the dual defect sites in graphite carbon nitride for ultra-high photocatalytic H<sub>2</sub>O<sub>2</sub> evolution. *Energy Environ. Sci.* **2022**, 15, 830-842.

Received: March 18, 2022

Accepted: April 30, 2022

Published: June 20, 2022